

ANALYSIS OF THIN CURVED FLEXIBLE STRUCTURES FOR SPACE APPLICATIONS

Sebastian Oberst¹, Doug Griffin¹, Sean Tuttle¹, Andrew Lambert¹ and Russell R. Boyce¹

¹School of Engineering and Information Technology, UNSW Canberra Space,
UNSW Australia, Canberra, ACT 2600, Australia
Email: s.oberst@adfa.edu.au

Abstract

With the advent of affordable nano-satellite designs (off-the-shelf payloads, standardised launch geometries), increasingly enterprises, governmental agencies and universities have started developing their own space programs to explore the environment of Low Earth Orbits. Thin, flexible and unfolding/deployable structures are common space engineering antenna and solar panel designs owing to their lightweight and ideal packaging characteristics, which are, however, difficult to experimentally validate in a 1-g environment. Further, curvatures or discontinuities to increase functionality without violating prioritised design criteria may lead to system-level trade-offs: stability issues arising from buckling in combination with micro-vibrations which feed back to the satellite's attitude behaviour. It appears that the literature lacks a systematic investigation of these aspects.

On-Earth experimental validations (static experiments, model updating) are the starting point for studying the response to static/dynamic loading of thin curved flexible structures such as deployable high frequency antennas. Linear and nonlinear buckling modes owing to varying loadings (aerodynamic drag, solar radiation pressure, residual gravity and magnetic body forces) are found together with a high sensitivity to torsional modes' frequency changes under micro-vibrational forcing.

1. Introduction

Nano-satellites such as cubesats, have become popular alternatives to conventional satellites with total launch costs being reduced to a few hundred thousand instead of millions of US\$ [1-3]. Thin elastic structures (TES) such as antennas, solar sails/panels including self-actuating hinges [4-7] play a key role in space applications owing to their light-weight, near to ideal packaging properties and their flexibility. However, performance enhancements of TES are often accompanied by increased energy demands, which again lead to larger but thinner solar panels owing to very stringent packaging restrictions in nano-satellites [8]. However, while operating in orbit, any satellite might be exposed to external and internal perturbations in form of environmental loads and impulsive thrusters, reaction wheels or magneto-torquers, respectively [9,10]. Especially in low earth orbits changing dynamic loads owing to rarefied atmosphere, altering solar radiation pressure or different strength of van Allen radiation have a strong influence on any TES. A sudden loss of moment of inertia or vibrational dissipation [6,11] may cause unwanted spacecraft tumbling [12,13] with the possibility of premature de-orbiting [14,15].

Hence, even though TES are especially suited for space applications they also need to be rigid, sufficiently flexible and able to sustain shocks or vibrations [16]. Flexible and deployable structures, similar in principle to those employed as space structures can be found everywhere in daily life

ranging from umbrellas and carpenter steel tape measures (tape springs) to foldable bar structures, bascule bridges and buildings [16,17]. Particularly, tape springs as thin continuous, elastically foldable metallic strips with a curved cross section have attracted much attention in space engineering [4]. Owing to an increased bending load capacity and rigidity [17,18], self-unfolding and -stabilising tape springs have been employed as hinges [16,19], parts of antennas [5] or even robot legs [20]. However, the modelling and analysis of tape springs as thin-walled slender and elastic structures needs to consider nonlinear behaviour [21] owing to geometrical instabilities and high sensitivities due to local cross-sectional folding [11]. Mansfield [22] highlights the problem of TES and their large displacements in aerospace applications and derived, therefore, analytical expressions of large-displacement relations for curved lenticular and constant thickness strips, which were able to display torsional and snap-through (nonlinear) buckling [22]. Seffen and Pellegrino [18] studied the dynamics of some tape spring deployment actuators and distinguished between (i) equal and (ii) opposite sense bending. The equal bending is characterised by two line contacts at the edges whereas the opposite bending is characterised by a single centred line contact when bent together. The folds owing to the “equal sense bending” become bi-stable for small rotation angles [23]. In the bistable situation two asymmetric equilibrium points exist, which can cause improper deployment in case of already very small gravity-induced effects and is accounted for the high imperfection loading/unloading sensitivity of the TES. Walker & Aglietti [8] found that for changed torsional (restoring) moments three-dimensional tape spring folds develop. The three-dimensional structure combines twisting and bending and results from asymmetric loading.

As mentioned before, in case of a failure of a thin elastic antenna, the spacecraft’s dynamics change. However, a rigorous experimental validation of the impact of the stability of a satellite attitude with a TES is difficult in a 1-g terrestrial environment due to the dominance of terrestrial gravitational forces and moments within the structure over the tiny in-flight disturbance forces and moments. Computational analyses of satellite dynamics are rather theoretical and strongly reduced in their complexity with many underlying assumptions especially with regards to realistic environmental loads; however, even experimentally validated updated models under terrestrial conditions are not extensively mentioned literature, which indicates a lack of systematic analysis. Especially for TES, the influence of structural nonlinearities and sensitivities to uncertainties in material composition, geometry, changing boundary conditions and varying loads is of paramount importance. Hence, we study for the purpose of a more complex vibration analysis an experimentally updated numerical model of a large tape spring antenna for its buckling behaviour. It assesses if the application of imperfections (e.g. varying thickness) or the change of loads under terrestrial and approximated space conditions might trigger buckling instabilities. A simplistic satellite structure is equipped with one TES to study the spacecraft’s dynamics under approximated loads as encountered in low earth orbits.

2. Experimental Model Updating

The TES is characterised by its geometry, boundary conditions and material properties via experimental model updating by applying the finite element package ABAQUS 6.14-2 (Standard) in combination with FEMTools 3.81. As TES common carpenter tape measures (‘Stanley 30-497’, length 5000 ± 0.2 mm, width 19.1 ± 0.2 mm, $N=9$) used as tape spring antennas are studied. Opposite bending the TES along its length and clipping it together at about 400 mm provides the *elastica* [17] with its average characteristic radius $r_c=19.1\pm 0.1$ mm ($N=9$), the average ‘deployment’ width of 17.5 ± 0.1 mm, a circle segment height of 2.75 ± 0.1 mm (Kincrome vernier calliper 2310). The angle is measured over the arc length S to be $2\beta=S/r_c=0.9947$ rads, (Fig. 1(a)). Three loading positions **A-C** are distinguished as depicted in Fig. 1(a). The painted tape spring was on average $t=0.1491\pm 0.0030$ mm thick (ball point-ended dial micrometer Mitutoyo PMUD 6-1” MJ389-37, $0.1 \mu\text{m}$ resolution) with a weight $w = 17.56 \pm 0.2$ mg/m and a mass density of $\rho=6197$ kg/m³. Stripping the paint off (solution of 87% CH₂ Cl₂, 13% CH₃OH) on $n=10$, $l=100$ mm segments (of $n=5$ carpenter measures), t and w reduced to $t=0.1128\pm 0.0061$ mm (-23.4%) and $w=16.75\pm 0.2$ mg/m (-4.6%), resulting in spring steel density of $\rho= 7815.42$ kg/m³. Owing to the tape spring being within the linear (small) deflection

regime ($< 6\%$ relative to a beam of length at $l=240$ mm) and rather stiff, the TES had a reduced (a) modal density and (b) buckling sensitivity compared to 1730 mm. However, the mass of the tape spring segment (3.5175 g) was too light for the force transducer (B&K 8200) available so that the force settings were calibrated by averaging the force spectra of a known circular aluminium plate (radius 30 mm, 1 mm thickness), which was validated with the spatially averaged acceleration spectrum multiplied by mass density in each point of an aluminium block, cf. [24].

In general, an accurate experimental characterisation of TESs is difficult as the boundary and loading conditions strongly influence the dynamics (nonlinearity and sensitivity): the structure is easily mass-loaded by miniature accelerometers and the excitation over shakers is easily (1) be too weak for the force transducers available owing to insufficient acceleration acting on a small mass or (2) the resulting vibration amplitudes are inhomogeneously spatially distributed resulting in either a locally reduced signal-to-noise ratio or an overdriven measurement system. Further, the TES tested here is basically a spring, which is considered to be weakly damped which would require a high frequency resolution in order to determine the modal damping.

Hence two setups **A** and **B** are suggested (both measured with a 45 mHz frequency resolution, 81 and 177 points with $n=15$ averages each): **A** has a 210 mm long TES to study the influence of the paint on the response and **B** with a TES of length 1730 mm, representative for a fully deployed antenna. The TES in setup **A** is excited via a B&K 4809 electro-dynamic shaker, in **B** the woofer of a loudspeaker is used (Radioshack Realistic Minimus-7, 8 Ohms, 40 W). The finite element model of a 625 mm long TES is mesh-independent using 2750 nonlinear SR6 shell elements.

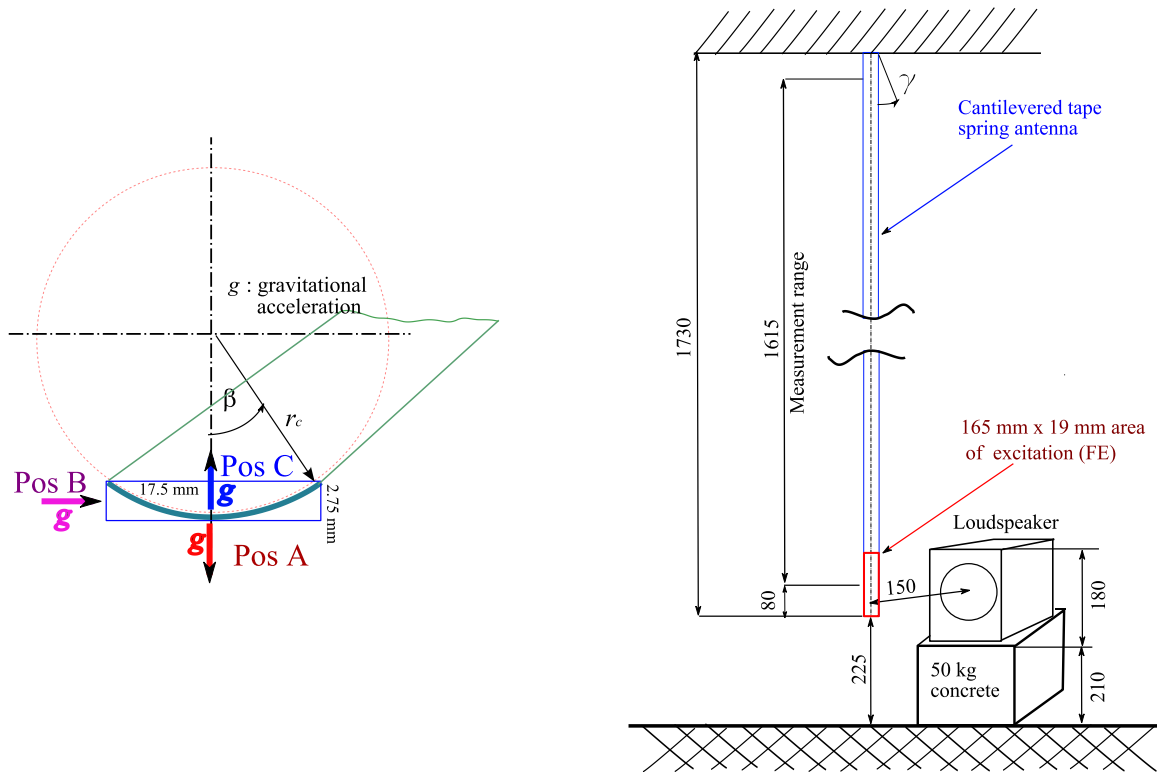


Figure 1. (a) Cross section, and positions A-C relative to gravity; (b) Experimental setup **B** to measure the damping & to conduct model correlation via FEM; the measurement range includes the grid points used for spatial averaging; the excitation area is only approximate (in mm).

The finite element mesh and the modal responses were imported into the model updating software FEMTools 3.8-1. A Polytec scanning laser vibrometer PSV-400-B (PSV-I-400 head, controller OFV-5000, PSV-E-401 junction box) was used to measure the response. Both setups were

connected to a B&K 2706 power amplifier and excited in loading position C (Fig. 1) of the TES to induce ‘equal sense bending’ [18]. Dynamic equal sense bending produced larger vibrations for smaller forces compared to opposite sense bending (Pos A).

Matching the experimental modes with a numerical modal analysis, gave an average modal assurance criterion of 85.4%. The updated material properties of the paint-stripped tape spring steel were $E = 201.12$ GPa (change to baseline +0.56%), and $\nu = 0.31$ (+26.7 %), the density was 0.11% higher than that determined over the weight and geometry measurements. The additional mass distribution caused by the paint influences stronger the higher bending and torsional modes (mean frequency change $\Delta f = 6.58 \pm 5.23$ Hz). In general, very little effect on the amplitude (i.e. damping) is observed with a mean amplitude change of about $\Delta A 0.62 \pm 0.55$ dB. For torsional modes, however, Δf and ΔA are more pronounced than for bending modes indicating a higher sensitivity to the changed mass distribution by stripping off the colour.

In order to determine a realistically damped numerical model all experimental modes within the frequency band of interest had to be identified and assigned to finite element (FE) modes for the full length TES of 1730 mm (setup B). The experimental velocity response spectrum could then be correlated to the FE response spectrum, and fitted using the nonlinear least squares method to determine the correct Rayleigh damping function [24,25]. The TES was glued to a metal rod (10 x 10 mm, 1 mm wall thickness), which was then bolted to a large steel frame as shown in Fig. 1(b). However, it was found that (1) the TES was not glued in a perfect 90° angle to the metal rod and (2) that the steel frame was slightly distorted using a digital inclinometer, which led to a total deviation of $1.75 \pm 0.2^\circ$ or 52 mm arc length as confirmed over a plumb (Fig. 1(b), $\gamma + 90^\circ \approx 91.72^\circ$). This deviation from 90° had to be accounted for in the gravitational terms in the numerical model. The vibrometer was setup at 3.74 m distance to capture about 93% of the length of the TES, as shown in Fig. 1(b). Due to the substantially reduced stiffness, higher modal density and associated higher buckling sensitivity it was difficult to identify an ideal dynamic range; the displacement at the top was $200 \mu\text{m}$ as compared to 1.6 mm at the end tip. A periodic chirp of 2 seconds attenuation time was the excitation signal; in order to limit the influence of gravity the TES was suspended vertically.

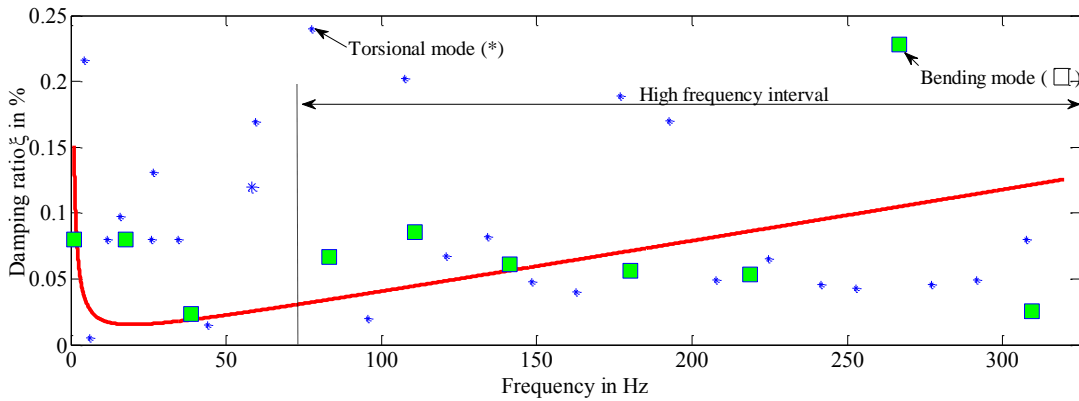


Figure 2. Rayleigh damping curve fitted via a nonlinear least square procedure using the experimentally extracted modal damping

However, also the loudspeaker excitation became problematic for distances below 100 mm relative to the TES’s tip as the loudspeaker’s magnetic field excited the tape spring’s ferrite steel and caused subsequently 0.8 Hz oscillations. Increasing the distance between the TES and the loudspeaker to about 150 mm and applying a 1 Hz high-pass filter (1) reduced the low frequency oscillations (2) and cleared the signal from residual low frequency noise. Owing to the loudspeaker’s characteristics (cut-off frequency 30 Hz), energy losses caused by the three dimensional diffuse acoustic sound field as excitation source and increasingly nonlinear response the coherence of the measurement dropped to about only 0.25 if excited below 75 Hz (low frequency interval) but recovered to about 0.8015 on average within 75 and 330 Hz (high frequency interval). However, in the low frequency interval it was

difficult to classify the torsional modes. Up to 80 Hz (coarser frequency resolution of 250 mHz, 29 nodes line segment, and ten averages) only the bending modes and above 80 Hz both, bending and torsional modes were used in the model updating process. After carefully identifying and matching the 31 of the 35 experimental modes (0- 312.5 Hz) with the 36 finite element modes (0 - 325 Hz), the modal damping at each frequency was identified with only about four mixed modes (3D bending & torsion) being experimentally not detected. These four missing modes were estimated and correlated to the FE modes via comparing the sequence of frequencies; their modal damping was estimated to be that of the average modal damping. The frequencies in the interval of 75-325 Hz of the bending modes were on average 3.16% higher and that of the torsional modes were 6.02% lower than those measured. The material properties differed on average by about +1.3 % to those of setup **A** due to the different number of matched modes (six compared to 17).

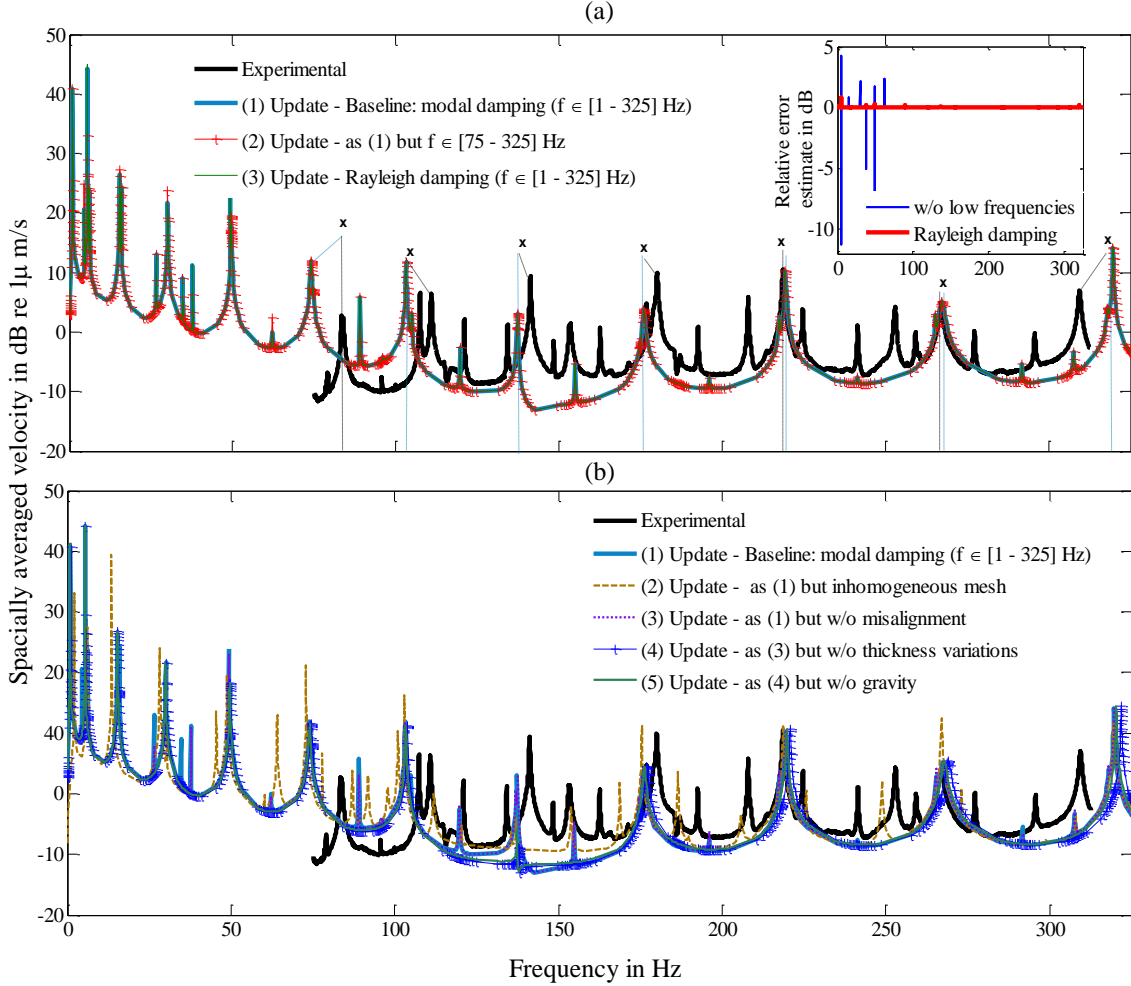


Figure 3: Spatially averaged velocity measurements for the 1730 mm tape spring; (a) comparing modal damping with and without (w/o) low frequency range to Rayleigh damping (with low frequency contribution), and (b) investigating the occurrence of torsional modes by introducing imperfections and varying load conditions; in (a) the insert gives an relative error estimate in dB for varving damping configurations. also indicated ('x') are the bending modes.

A Rayleigh damping function ξ was fitted to the experimentally extracted modal damping values by applying a nonlinear least squares fitting procedure [24, 25] as depicted in Fig. 2, to the equation.

$$\xi = \frac{\alpha}{2\omega} + \frac{\omega\beta}{2} \quad (1)$$

with $\alpha = 0.01898$ and $\beta = 1.24 \times 10^{-6}$ being the mass and the stiffness proportional damping parameters. Apart from being as expected weakly damped, the stiffness proportional damping factor dominates, both being expected from spring steel [26, 27].

Using the updated material properties, Fig. 3 compares the experimentally obtained spatially averaged high-frequency response with the computationally generated velocity magnitude in out-of-plane direction: for (a) with different damping values and (b) with imperfections and changed preloads. The excitation in the finite element models was set to a pressure with a resultant of $2.82 \mu\text{N}$ ($\sim 80.5\%$ based on averaged coherence value) taking into account $\gamma = 1.72^\circ$. As can be seen from Fig. 3(a) and its insert (relative error estimate to baseline model due to changed damping) the forced response requires careful extraction of modal damping values. Only if sufficient modal damping values are (1) extracted and (2) matched the extraction of Rayleigh damping over the whole frequency range is possible with a low average relative error as indicated by the insert of Fig. 3(a).

The FE model only reflects the bending modes of the spring tape properly (indicated by ‘x’). The torsional modes resonances are rather weak. Increasing the asymmetry of the loading and introducing imperfections in form of uniformly distributed average thickness ($\mu \pm 3\sigma = 0.1128 \pm 0.0183 \text{ mm}$) and an asymmetric mesh (unstructured meshing, non-symmetric seeding) triggers the response of the torsional modes to increase as indicated in Fig. 3(b). The response level is approximately correct, which reflects on a properly determined force magnitude of excitation damping and the numerical bending modes are well within frequency range of the experimental data. However, it was already highlighted that the updating process based, on comparing the experimental response with the numerical response did not work well for the torsional modes. This is not really astonishing, considering the large frequency range, the nature of the structure as a very thin flexible nonlinear structure with high imperfection sensitivity and the number of modes included. Residual stresses due to the manufacturing of the heat-treated spring tape are also not modelled in ABAQUS. However these stresses are very influential especially on the appearance and strength of the torsional vibration modes. The excitation over a loudspeaker is not ideal, as the sound field is reflected, the excitation is asymmetric and rather uncontrolled and wavelength dependent. It is hence a rather complex task to reproduce this type of excitation in the FE model. Additionally, the paint of the whole spring tape should be stripped off in order to further reduce its effect on the response spectrum.

3. Static Stability Analysis and its Effect on the Motion of the Satellite

With the experimentally updated tape spring model at hand, a static stability analysis is conducted to test whether a fully deployed tape spring antenna is stable under terrestrial and under space conditions. By first applying a quasi-static nonlinear stress analysis, in a second step the proportionality factor hence the critical buckling loads F_{cr} are calculated. The critical buckling loads form buckling instability margins (BIM), which are represented by hyperbolas for the non-prestressed cases. Various buckling modes such as torsional modes, snap-through bending modes or combinations of thereof can be found. In loading position A (path ‘origin – 1 – 3’, opposite sense bending in Fig. 4), a snap – through analysis (nonlinear buckling or Riks analysis) had to be conducted. In loading position C (path ‘origin – 2 – 3’, equal sense bending in Fig. 4) a linear buckling analysis worked find. In point 2 of Fig. 4 exists a bistable solution [8]: Having only gravity acting, the TES remains in an unstable equilibrium and loses gradually load capacity, before a total loss of stability occurs (point 3 in Fig. 4). Position B is the most complicated to analyse as being marginally stable per se: the tape spring will either directly lose stability by twisting into Pos C and buckle or twist into position A. While the motion in position C immediately destabilises the structure, turning into position A, gives a kind of tertiary structure, which acts in fact stabilising.

3.1 Terrestrial conditions

Figure 5(a) investigates numerically the BIMs for of Pos A-C (Fig. 1(a)) as well as that for a straight profile steel beam under $1 g$ terrestrial loading. For Pos A $n=4$ spring tapes are experimentally studied

and their mean value is taken in order to validate the numerical calculations. The spring tape is loaded at the tip with discrete brass weights of 5, 10, 20, 50 g as well as 5 x 5 mm² fridge magnet cut-outs (0.13 ± 0.08 g) until ‘snap through buckling’ occurred (position 3, Fig. 4). The uncertainty corridor is calculated once but then used for Pos A-C by assuming normally distributed critical loads at each TES length in Pos A and taking its standard deviation. The standard deviation is then added to the BIM’s standard deviation originating from thickness variations (only numerical calculations). Experimentally, the tape spring in Pos A buckles only after a length of 1730 mm with all $n=4$ tape springs being stable at this length having a residual load capacity of $F_{cr} = 5.674 \pm 2.74$ mN. The numerical computations for Pos A using the updated material properties from Section 2 match very closely the experiments and cross the uncertainty bounds only for lengths greater than 1700 mm; the longer the tape spring the more the uncertainty corridor is dominated by the finite resolution of the incrementally added weights. The failure-length of Pos C is with 736 mm much higher than that of the straight steel tape, but it is much lower than that found for Pos B (1026 mm) and Pos A (>1730 mm), and is within reach of the experimental maximum buckling length of about 688 ± 17 mm ($n=30$).

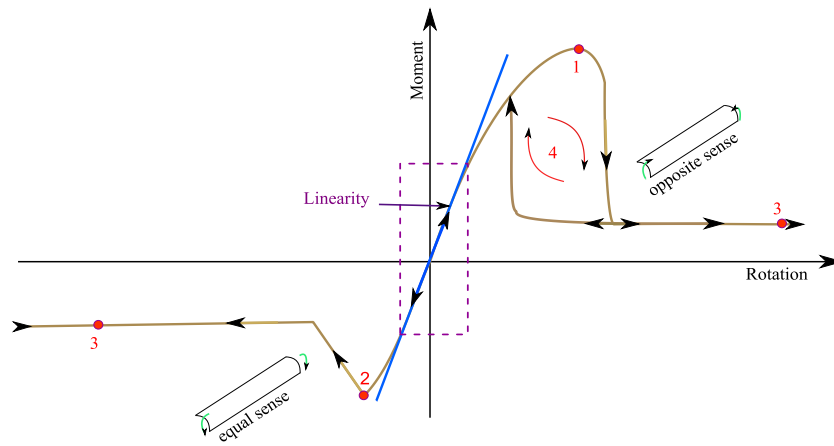


Figure 4: Schematic of moment-rotation relationship for tape springs greater than 250 mm (nonlinear ‘large deflection’) cf. [14]; (1) opposite sense bending (first quadrant): after linearly increasing, the tape spring deflects largely then ‘snaps-through’ (Riks analysis, nonlinear buckling) at point ‘1’, loses immediately stiffness, then a constant ‘steady-state moment’ ‘3’ sets in; reducing the angle again gives to hysteresis; (2) equal sense bending the maximum moment is far lower and very quickly the system buckles ‘2’ (linear buckling due to a bifurcation and bi-stability (torsional mode), then the moment decreases quickly to the ‘steady-state’ moments ‘3’.

3.1.1 Space environment

Next the finite element model is used to simulate the stability behaviour of the spring tape in Pos C as the least stable position exposed to a combination of environmental loads as encountered in low earth orbits (LEO). Here, the (1) aerodynamic (AP) and the (2) solar radiation pressure (SRP), as well as body forces owing to (3) residual micro-gravity and (4) electro-magnetism (van Allen radiation belts) are considered. The aerodynamic pressure P_a is calculated over

$$P_a = \frac{1}{2} c_d \rho v^2 = 4.47E-3 \text{ N/m}^2. \quad (2)$$

Here, $c_d = 2.85$ is the assumed lateral drag coefficient at low solar activity (average) of a box considering an orbital and a thermal speed as encountered for orbits of 400 – 800 km height [28]; especially it is considered that above 500 km the drag coefficient increases, due to (1) a change in the atmospheric composition from being N molecule dominated to oxygen molecules in the thermosphere and (2) to the violation of the hyper-thermal flow assumption [28,29]. The density ρ at about 400 km height (hyper-thermal flow) is assumed to be rarefied with either $\rho = 5.04 \text{ E-}11 \text{ kg/m}^3$ for increased solar activity or $\rho = 3.89E-12 \text{ kg/m}^3$ in case of mean solar activity [28-30]. The average relative speed

of a spacecraft in-orbit is calculated to be $v = \sqrt{GM/r}$ in $[7.65, 7.89] \pm [0.0383, 0.0395]$ km/s; here G and M being the universal gravitational constant (not considering its variation [31]) and the earth's mass but neglecting the mass of the spacecraft. For P_a the resultant force is $F_a = 0.147$ mN.

The solar radiation pressure P_{SR} and its resultant force F_s are calculated considering the light's absorption and reflection using the so-called 'cannonball model' [32]

$$P_{SR} = \frac{\Phi}{c} \left(1 + \frac{4}{9}\delta\right) = 8.69\text{E-}6 \text{ N/m}^2, \quad (3)$$

with $\Phi = 1850 \text{ W/m}^2$ being the solar flux at 800 km (1375 W/m^2 at 400 km) distance to the earth, $c = 299,792,458 \text{ m/s}$, being the speed of light and $\delta = 0.92$ being the sum of the specular and diffuse reflection coefficients of gold foil as the worst case [32]. For P_{SR} the resultant force is $F_s = 2.85\text{E-}4 \text{ mN}$. Furthermore, body forces

$$F_{\mu g} = 2.5\text{E-}6 \text{ g } m = 0.02453 \text{ mN} \text{ and} \quad (4)$$

$$F_{em} = q(E + vB) = 3.49 \text{ E-}4 \text{ mN} \quad (5)$$

owing to μ -gravity ($F_{\mu g}$, with $g = 9.81 \text{ m/s}^2$) [33,34] and electromagnetic attraction as exerted by e.g. the van Allen radiation belts act on the orbiting spacecraft. Here, $B = 0.3\text{E-}4 \text{ kg/Cs}$ [35] being the magnetic field and $E = 400 \text{ mV/m}$ being the maximum electric field magnitude observed in van Allen probes [36,37]. The charge of the spacecraft ($q = 6\text{E-}7 \text{ C}$) is calculated assuming 1000 V as peak voltage of the satellite [36-38].

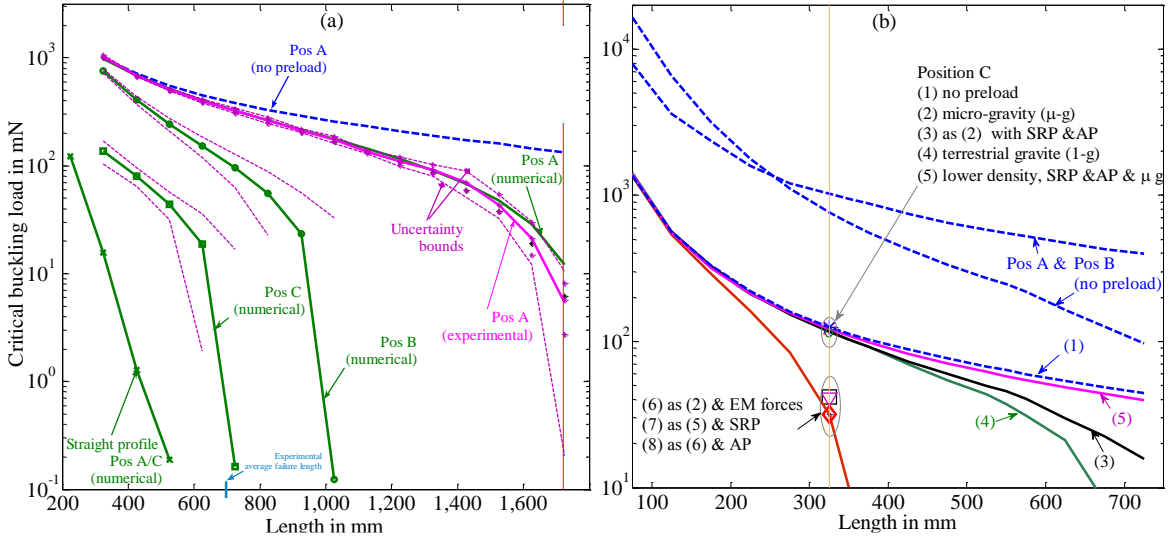


Figure 5: (a) Experimental BIM taken as average ($n=4$) with its uncertainty corridor for pos A; computational data for pos B and C as well as for a straight profile are also included; the uncertainty stems mainly from the standard deviation of using incremental loads in the experiments. The lowest maximum load of Pos B and C can be found at about 1025 mN and 680 mN, respectively; as expected the straight profile takes far less load than the spring tape structure; (b) critical loads for Pos C (without any preloads as benchmark for Pos A-C as dashed line); various load scenarios as potentially encountered in low earth orbits indicate the high sensitivity of the spring tape to even very small loading conditions.

The results of the static stability analysis on the tape spring as depicted in Fig. 5(b) indicates that applying the aerodynamic and the solar radiation pressure gives a larger BIM than under terrestrial conditions for Pos C. Taking into account electromagnetic body forces aggravates the situation considerably. Reducing the air density owing to a mean solar activity increases the stability but finally leads to buckling at about 1510 mm.

It can be summarised that the effects of (1) different preloads, (2) the sum of different forces acting, and (3) the direction of the applied buckling load are not proportional to critical loads or give a significantly different stability region. This is due to the strong nonlinearity and high sensitivity of the structure. Hence, even though the curved tape spring is much stronger than its straight counterpart, its deflection even for rather small loads becomes large leaving the zone of linear Euler-Bernoulli beam approximations (Schematic Fig. 4). However, all loads as calculated here can only serve an approximation for loads as encountered in space and are associated with large uncertainties. Research on the electromagnetic field as exposed by the Van Allen belts is still in its infancy stage. Also, e.g. the density ρ of the air is not only depending on the distance to earth but also on the solar activity, predictions of ρ are found to underestimate the density by 15% for low solar intensity and up to 30-50% at high solar activity [28]. Only a mission in space with experimentally measured forces on the TES could validate results presented here.

Next a transient nonlinear time domain analysis is conducted using ABAQUS Explicit 6.14-2. The loads determined in Section 3 but without the electromagnetic body force are applied to a simplistic satellite model with two tape springs. The body of the spacecraft is made of solid material with the mass of 1.33 kg ($100 \times 100 \times 100 \text{ mm}^3$) with the Young's modulus and Poisson's ratio being that of aluminium (70 GPa & 0.28). The two elastic structures are not connected to each other but tied to the nodes of the satellite body. The spacecraft has in total 3196 nodes (64 C3D8I ABAQUS/Explicit elements for the satellite body and 1566 S4R linear shell elements) and is exposed to a constant field of μ -gravity. The AP and SRP (as calculated in section 3) act perpendicular to only one elastic structure in the equal bending sense and on one side of the satellite body perpendicular to μ -gravity (red in Fig. 6(a)). As the load increases, the elastic structure starts to buckle at around 0.50 s (Fig. 6(b)). As a consequence of the failure of the tape spring the satellite changes its position suddenly and rotates about its x -axis and y -axis as depicted in Fig. 6(b) for the instantaneous rotation (difference between undeformed and deformed structure).

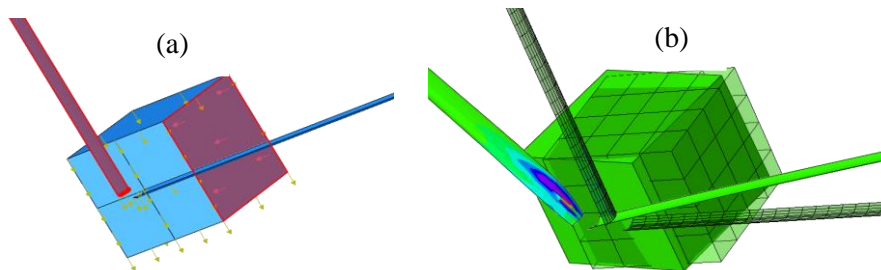


Figure 6: The satellite structure (a) being ramp loaded with aerodynamic and solar radiation pressure (in red) and μ -gravitation; and in (b) after application of the loads at $t=1.0$ s the buckled structure, and its stresses on the deformed structure, its displacement relative to the undeformed.

4. Conclusions

Numerical models of spring tape antennas are here experimentally updated in order to test their stability and in case of a failure their impact on a generic satellite model. Owing to imperfections such as thickness variations, asymmetrical loading an asymmetrical mesh, resonances of torsional modes appear in the velocity response spectrum possibly due to high sensitivity of thin, elastic structures (TES) to stress gradients. The dynamic updating of the thin elastic structure as tested here was very difficult. In case of the spring tape antenna used the numerical model should include the material's residual stress distribution owing to heat treatment in course of the manufacturing process. The forcing over a loudspeaker is not ideal the acoustic waves presumably excite the torsional modes more than a mechanic shaker would, owing to reflections, near field effects, local sound pressure differences and wavelength dependent coupling to the structure. A non-contact and precise point excitation as over ultrasonic interference exciter using the ultrasonic radiation force should be developed for the purpose of testing thin elastic structures. Conducting a static stability analysis using both a linear and nonlinear

buckling (snap-through) analysis for terrestrial gravity gave however well matching numerical and experimental buckling instability margins (BIM). The critical load curve varies for the buckling forces being either applied in opposite, equal sense bending or ‘sideways’ (at the centre of the spring tape’s tip) tangential to the spring tape’s curvature. Applying approximated space loads via a static nonlinear stability analysis indicates that the structure buckles sooner than under terrestrial conditions if electromagnetic forces are considered. As the deployment length of the TES increases, it will have a greater propensity to become unstable under adverse loading aerodynamic, solar radiation and micro-gravity conditions. This is also true for a lower density assumption at mean solar activity where the analysis indicates that the TES could buckle at about 87% of the chosen maximum length. As indicated by a transient analysis, the equal side bent tape spring antenna buckles and may initiate tumbling of the satellite. It is shown that owing to failure and a sudden loss of inertia and imbalance in the external loads, a disturbance torque will be imposed on the spacecraft. If this is not fully compensated by the attitude determination and control system, the spacecraft will start to tumble. However, it has to be mentioned that the true environmental loading in space is unknown. A complete validation of the dynamic behaviour in space is only possible by monitoring the stability and vibrations of the antennas for in-space/ in-orbit missions.

References

- [1] Toorian A, Diaz K, Lee S, Aerospace Conference, 2008 IEEE, p1-14, 1-8 March 2008
- [2] Isar A, “Vibration and modal analysis of low earth orbit satellite”, Shock and Vibration, Volume 2014, ID 740102, 8p
- [3] Piattoni J, Candini GP, Pezzi G, Santoni F, Piergetili F, “Plastic Cubesat: An innovative and low-cost way to perform applied space research and hands-on education”, Acta Astronautica, 81:412-429 (2012).
- [4] Patel J, Ananthasuresh GK, “A kinematic theory for radially foldable planar linkages”, International Journal of Solids and Structures, 44:6279-6298 (2007).
- [5] Soykasap Ö, Pellegrino S, Howard P, Notter M, “Folding large antenna tape spring”, Journal of Spacecraft and Rockets, 45: 560 -567 (2008)
- [6] Sokolowski WM, Tan SC, “Advanced Self-deployable structures for space applications”, Journal of Spacecraft and Rockets, 44: 750- 754 (2007).
- [7] Mathers N, Thompson L, “Using inflatable antennas for portable satellite-based personal communication systems”, Acta Astronautica, 61:659-663 (2007).
- [8] Walker SJI, Aglietti GS, “Experimental Investigation of Tape Springs Folded in Three Dimensions”, AIAA Journal, 44(1), 151-159 (2006).
- [9] Candini GP, Piergentili F, Santoni F, “Miniturized attitude control system for nanosatellites”, Acta Astronautica, 81: 325 – 334 (2012).
- [10] Zhang Z, Aglietti GS, Ren W, “Coupled microvibration analysis of a reaction wheel assembly including gyroscopic effects in its accelerance”, Journal of Sound and Vibration, 332: 5748-5765 (2013).
- [11] Guinot F, Bourgeois S, Cochin B, Blanchard L, “A planar rod model with flexible thin-walled cross-sections. Application to the folding of tape springs”, Int. Journal of Solids and Structures, 49: 73-86 (2012).
- [12] Bracewell RN, Garriott OK, “Rotation of artificial earth satellites”, Nature, 182: 760-762 (1958).
- [13] Gale AH, Likins PW, “Influence of flexible appendages on dual-spin spacecraft dynamics and control”, Journal of Spacecraft, 7:1049-1056(1970).
- [14] Mengali G, Quarta AA, Romagnoli D, Circi C, “H2-reversal trajectory: A new mission application for high-performance solar sails”, Advances in Space Research, 48:1763-1777 (2011).
- [15] Tekinalp O, Atas O, “Attitude control of satellites with de-orbiting solar sails”, IEEE, 347-351 (2013).
- [16] You Z, Pellegrino S, “Foldable Bar Structures”, International Journal of Solids and Structures, 34: 1825-1847 (1997).
- [17] Petroski H, “Deployable Structures”, American Scientist,92:122-126 (2004)
- [18] Seffen KA, Pellegrino S, “Deployment dynamics of tape springs”, Proceedings of the Royal Society of London, Series A: Mathematical and Physical Sciences, 455, 1003-1048, (1999).

- [19] Hoffait S, Brüls O, Granville D, Cugnon F, Kerschen G, “Dynamic analysis of the self-locking phenomenon in tape spring hinges,” *Acta Astronautica*, 66, 1125-1132 (2010).
- [20] Aridon G, Remond D, Morestin F, Blanchard L, Dufour R, “Self-deployment of a tape-spring hexapod: experimental and numerical investigation”, *Transactions of the ASME*, 131: 021003-1 to 021003-7 (2009).
- [21] Soykasap Ö, “Analysis of tape spring hinges”, *International Journal of Mechanical Sciences*, 49, 853-860 (2007).
- [22] Mansfield EH, “Large-deflexion torsion and flexure of initially curved strips,” *Proceedings of the Royal Society of London, Series A: Mathematical and Physical Sciences*, 334: 279-298 (1973).
- [23] Seffen KA, You Z, Pellegrino S, “Folding and deployment of curved tape springs”, *International Journal of Mechanical Sciences*, 42, 2055-2073 (2000).
- [24] Zhang Z, Oberst SM, Williams JJR, Lai JCS, “Improving brake squeal propensity prediction by model updating,” *Acoustics 2015*, 15-18 Nov, Hunter Valley, Australia (2015).
- [25] Williams JJR, Zhang Z, Oberst SM, Lai JCS, 2015, “Model updating of brake components’ influence on instability predictions”, presented at ICSV22, Florence, Italy, 12 - 16 July 2015.
- [26] Orban F, “Damping of materials and members in structures”, *Journal of Physics* 268 (2011) 012022.
- [27] Pérez-Peña A, García-Granada AA, Menacho J, Molins JJ, Reyes G, “A methodology for damping measurement of engineering materials: application to a structure under bending and torsion loading”, *J Vibration Control*, 1-11, (2014).
- [28] Pardini C, Anselmo L, “Comparison of thermospheric density models by satellite orbital decay analysis”, IAF-00-A.5.01, AIAA, 2000.
- [29] Vallado DA, Finkleman D, “A critical assessment of satellite drag and atmospheric density modelling”, Paper AIAA 2008-6642, AIAA/AAS Astrodynamics Specialist Conference & Exhibit, Honolulu, Hawaii, USA, 18 – 21 Aug.
- [30] www.braeunig.us/space/atmos.htm
- [31] Anderson JD, Schubert G, Trimble V, Feldman MR, “Measurements of Newton’s gravitational constant and the length of the day”, *A Letters Journal Exploring the Frontiers of Physics*, 110: 10002-p1-p5 (2015).
- [32] Kubo-oka T, Sengoku A, ‘Solar radiation pressure model for the relay satellite SELENE’, *Earth Planets Space*, 51: 979-986 (1999).
- [33] Pletser V, Short duration microgravity experiments in physical and life sciences during parabolic flights: the first 30 ESA campaigns, *Acta Astronautica* 55: 829- 854 (2009).
- [34] Benz KW, Dold P, ‘Crystal growth under microgravity: present results and future prospects towards the International Space Station’, *Journal of Crystal Growth* 237-239: 1638 – 1645 (2002).
- [35] Sehnal L, “The motion of a charged satellite in the earth’s magnetic field”, *Smithsonian Astrophysical Observatory, SAO Special Report #271*, (1969)
- [36] Kellogg PJ, Electrons of the Van Allen Radiation, *Journal of Geophysical Research*, 65 (9), 2705 – 2713.
- [37] Li W, Ma Q, Thorne RM, Bortnik J, Kletzing CA, Kurth WS, Hospodarsky GB, Nishimura Y, ‘Statistical properties of plasmaspheric hiss derived from Van Allen Probes data and their effects on radiation belt electron dynamics, *Journal of Geophysical Research: Space Research*, 10.1002/2015JA021048
- [38] Mozer FS, Bale SD, Bonnell JW, Chaston CC, Roth I, Wygant J, Megavolt parallel potentials arising from double-layer streams in the Earth’s Outer radiation belt, *Physical Review Letters*, 111: 235002 (2013).